



## Full length article

# Highly sensitive and selective label-free detection of dopamine in human serum based on nitrogen-doped graphene quantum dots decorated on Au nanoparticles: Mechanistic insights through microscopic and spectroscopic studies

Ruma Das<sup>a</sup>, Kamal Kumar Paul<sup>a</sup>, P.K. Giri<sup>a,b,\*</sup><sup>a</sup> Department of Physics, Indian Institute of Technology Guwahati, Guwahati 781039, India<sup>b</sup> Centre for Nanotechnology, Indian Institute of Technology Guwahati, Guwahati 781039, India

## A B S T R A C T

A rapid, facile and label-free sensing strategy is developed for the detection of dopamine (DA) in the real samples by exploiting nitrogen-doped graphene quantum dots (N-GQDs) decorated on Au nanoparticles (Au@N-GQD). The as-grown Au@N-GQD exhibits strong blue fluorescence at room temperature and the fluorescence intensity is drastically quenched in presence of DA in neutral medium. The mechanistic insight into the DA sensing by Au@N-GQDs is explored here by careful monitoring of the evolution of the interaction of Au NPs and N-GQDs with DA under different conditions through electron microscopic and spectroscopic studies. The highly sensitive and selective detection of DA over a wide range is attributed to the unique core-shell structure formation with Au@N-GQD hybrids. The quenching mechanism involves the ground state complex formation as well as electron transfer from N-GQDs. The presence of Au NPs in Au@N-GQD hybrids accelerates the quenching process (~14 fold higher than bare N-GQDs) by the formation of stable dopamine-o-quinone (DQ) in the present detection scheme. The fluorescence quenching follows the linear Stern-Volmer plot in the range 0–100  $\mu\text{M}$ , establishing its efficacy as a fluorescence-based DA sensor with a limit of detection (LOD) 430 nM. Further, based on the systematic change in the intensity of absorption peak of Au@N-GQD with DA concentration, the well-known Hill equation is introduced for the sensing of DA in the range 0–10  $\mu\text{M}$  with detection limit 40 nM. The proposed sensing method has a high selectivity towards DA over a wide range of common biological molecules as well as metal ions. The quenching in Au@N-GQD fluorescence intensity makes it possible to determine the spiked DA in human serum in the linear range from 0.0 to 80.0  $\mu\text{M}$  with the limit of detection (LOD) 590 nM, which is ~27 fold lower than the lowest abnormal concentration of DA in serum (16  $\mu\text{M}$ ). This sensing scheme is also successively applied to trace DA in Brahmaputra river water sample with LOD 480 nM including its satisfactory recovery (95–112%). Our studies reveal a novel sensing pathway for DA through the core-shell structure formation and it is highly promising for the design of efficient biological and environmental sensor.

## 1. Introduction

Dopamine (DA) is an important catecholamine neurotransmitter, which plays an important role in the mammalian central nervous system to send the signal from body to brain. Renal, hormonal, cardiovascular systems are also controlled by the normal level of DA [1]. Normal level of DA in body maintains blood pressure, fine motor activity, inspiration, intuition and focus, while, the dysfunction of DA has been implicated in pathogenesis of neurological disorders such as Huntington's disease, Schizophrenia and Parkinson's disease [2–5]. Thus, a precise detection of DA with high sensitivity and selectivity is of great interest for the clinical diagnosis of neurological diseases. Various sensing methods have been developed for the detection of DA including the high-performance liquid chromatography [6], capillary electrophoresis [7], electrochemical [8], fluorescent sensors [4,9] and colorimetric sensor [3]. Among these, colorimetric and fluorescence sensing

methods are regarded as the simplest as well as cost and time effective methods with appreciably lower detection limit.

In recent times, the unique physical and electronic properties of graphene and its derivatives have drawn a vast attention in diverse research areas with novel applications [10–12]. Graphene quantum dots (GQDs), a zero-dimensional material with  $\text{sp}^2$ -hybridized carbon derived from graphene, have received intensive attention in sensing applications due to its interesting intrinsic properties, such as low cytotoxicity, favorable biocompatibility and excellent optical properties including photo-stability, anti-photobleaching, intensive photoluminescence (PL) and ultraviolet absorption caused by the quantum confinement effect and excessive functional groups at the edges or basal planes of GQDs [13–15]. By the doping of heteroatoms into the  $\pi$ -conjugated system of GQDs, structural defects are introduced to make more active sites available in GQDs [16]. Sung et al. demonstrated the synthesis of nitrogen-doped GQDs (N-GQDs) possessing high active sites

\* Corresponding author at: Department of Physics, Indian Institute of Technology Guwahati, Guwahati 781039, India.  
E-mail address: [giri@iitg.ac.in](mailto:giri@iitg.ac.in) (P.K. Giri).

and exhibiting interesting properties [17]. The PL property of GQDs has been used for the detection of DA through its intensity quenching (down to 0.25  $\mu\text{M}$ ) [15]. Chen et al. recently reported DA sensing with N-GQDs up to 1  $\mu\text{M}$  concentration [9]. For the detection of DA, metallic nanoparticles (NPs) were also used as a promising detector and mainly aggregation of the NPs in presence of DA has been reported to be the key sensing factor [2,3,18]. Gold nanoparticles (Au NPs) combined with graphitic materials are highly promising for sensing applications. The oxygen-rich functional groups on the surface of graphene provide active sites for the nucleation of Au NPs instead of the use of conventional reducing agents [14,19]. Following this unique synthesis method, the GQD functionalized Au NPs were prepared for the various sensing applications including metal ion sensing [20],  $\text{H}_2\text{O}_2$  sensing [21], etc. Recently, reduced GQDs with Au NPs core-shell structure has been used for the colorimetric detection of cysteine by aggregation [14]. Though a variety of sensing methods have been developed for DA with high sensitivity and selectivity, an in-depth understanding of the sensing mechanism is lacking. Lin et al. reported colorimetric DA sensing through the aggregation of Ag NP by Ag-catechol bonds formation [3]. In another study on the colorimetric detection of DA, it was reported that in presence of  $\text{Cu}^{+2}$  ion, DA is adsorbed on Au NP surfaces after interacting with  $\text{Cu}^{+2}$  ion by its amino and hydroxyl groups [2]. Through FRET process, DA detection has been reported with the quenching of PL based on the formation of polydopamine on the surface of GQDs [22]. N-GQDs were also introduced for DA sensing, where electron transfer from photoexcited N-GQDs to dopamine-quinine has been pointed out as the reason of PL quenching [9]. Qu et al. mixed carbon dots with Au NPs for the detection of DA by the change of PL and chemisorptions interaction by the amine groups of DA and H-bond formation were reported as the detection mechanism [23]. To the best of our knowledge, there is no report on the optical based sensing of DA by N-GQD functionalized Au NPs (Au@N-GQD) through the formation of core-shell like structure with DA.

In this present work, we develop a rapid, stable, sensitive and highly selective sensor for the optical detection of DA using Au@N-GQD with low technical demands. Au@N-GQD was prepared by a one-step chemical reduction of  $\text{AuCl}_4^-$  in an aqueous N-GQD medium. In neutral aqueous medium, oxygen-rich functional groups on N-GQDs facilitate the complex formation with DA, which in turn facilitates the formation of a core-shell structure with DA as shell over Au NPs core. Mechanism of sensing is revealed through the detailed microscopic and spectroscopic studies. Based on the phenomenon of complex formation, this newly developed optical sensor is used for the efficient detection of DA through the measurement of UV–Vis absorption as well as the fluorescence quenching. An ultra-high detection limit for DA is achieved with the continuous enhancement in UV–Vis absorption intensity with DA concentration, which is found to follow the well-known Hill equation. The Au@N-GQD shows superior performance as a fluorescence sensor as compared to the bare N-GQDs, and it follows the linear Stern-Volmer equation. Additionally, this sensor has been applied for the detection of DA in the real samples, such as Brahmaputra river water and human serum with LOD 480 nM and 590 nM, respectively, with high selectivity as well as recovery.

## 2. Materials and methods

### 2.1. Synthesis of graphene oxide

At first, the graphene oxide (GO) was synthesized from graphite flakes by the modified Hummers method [24]. In a typical synthesis, 3 g expandable graphite flakes (purity 99%) and 1.5 g  $\text{NaNO}_3$  were added to 70 mL of concentrated  $\text{H}_2\text{SO}_4$  (98%, Merck) and mixed under stirring for 2 h. Next, the mixture was transferred into an ice bath and 9 g of  $\text{KMnO}_4$  (Merck) was added slowly under stirring. Then the stirring was continued at 35  $^\circ\text{C}$  for 4 h to allow proper oxidation of graphite. Deionized water (DI) was slowly added to the mixture and stirred at 98  $^\circ\text{C}$ .

The solution was then quenched with 15 mL of 30%  $\text{H}_2\text{O}_2$  (48%, Merck). Afterward, 60 mL HCl (35%, Merck) was mixed with it slowly and kept under stirring for 4 h to remove unreacted  $\text{NaNO}_3$  and  $\text{KMnO}_4$ . DI water was added to the mixture to dilute the acidic content. Later, with centrifugation at 10,000 rpm for 10 min in 3 cycles, the solution was separated from the unreacted flakes and impurities. The precipitated part was dried at 120  $^\circ\text{C}$  and collected as GO powder.

### 2.2. Synthesis of N-GQDs

N-GQDs were synthesized by a solvothermal method using GO as the precursor material. 600 mg of GO powder was dispersed in 40 mL of DMF (99%, Sigma-Aldrich) and sonicated for 30 min. The mixture was transferred into Teflon lined autoclave (Berghof, BR-100) and heated at 220  $^\circ\text{C}$  for 5 h. After the solvothermal treatment, the black precipitate was rejected after centrifugation and the yellow suspension was collected as N-GQDs. The solvent was evaporated by heating at 90  $^\circ\text{C}$  and N-GQDs are re-dispersed in Milli-Q water (18.3  $\text{M}\Omega\text{ cm}$ , MQ water), following its preservation at 4  $^\circ\text{C}$ .

### 2.3. Synthesis of Au@N-GQD

14 mg of as-synthesis N-GQDs was dispersed in 20 mL MQ water in ultra-sonication. Then the solution was heated at 110  $^\circ\text{C}$  with stirring for 10 min. Afterward, 2 mg of  $\text{HAuCl}_4$ , 4  $\text{H}_2\text{O}$  solution (5 mM, 99.9%, Alfa Aesar) was added dropwise into the above solution. The yellow colour of the solution containing N-GQDs is observed to be changed into a light pink colour, which indicates the formation of Au@N-GQD. After the natural cooling to room temperature, the Au@N-GQD was collected as a precipitate by centrifugation at 13,000 rpm for 10 min. The concentration of the obtained Au@N-GQD solution is 0.63 mg/mL. N-GQDs with a concentration of 0.09 mg/mL have been used as the control sample (N7). Au@N-GQD aqueous solution at a concentration of 0.09 mg/mL has been used for most of the experiments and the sample is termed as A7. For comparison, higher and lower concentrations of Au@N-GQD aqueous solution were used and these are termed as A5 and A9 for concentrations 0.126 and 0.07 mg/mL, respectively. In addition, Au@N-GQD was prepared with other amounts of N-GQDs (i.e. 4, 6, 10 and 20 mg) using the same conditions and treatment procedures as above.

### 2.4. Sensing of dopamine

The detection of dopamine (DA, Sigma Aldrich) was performed in PBS buffer solution at pH 7. For the efficient sensing of DA, different concentrations of stock solution of Au@N-GQD were used to find out the optimum concentration and repeatability for the sensing. In a typical run, 0.5 mL of stock solution of Au@N-GQD and 2.0 mL of DA solutions at different concentrations, ranging from 0.01 to 100  $\mu\text{M}$  are added into a cuvette and incubated for 4 min at 30  $^\circ\text{C}$  temperature before taking the absorption and PL spectra. All PL spectra are recorded under the excitation at 300 nm. All the measurements were repeated thrice to ensure accuracy. For the comparison, UV–Vis absorption and PL spectra of bare N-GQDs (N7) were also recorded.

### 2.5. Characterization techniques

Transmission electron microscope (TEM) including high-resolution TEM and selected area electron diffraction (SAED) pattern were obtained from JEOL-JEM 2010 transmission electron microscope operated at 200 kV for the high magnification surface morphology and structures. The test sample was obtained by drop-casting the aqueous dispersion on a carbon-coated copper grid of 400 mesh (Pacific Grid, USA), followed by drying at 50  $^\circ\text{C}$  temperature. Atomic force microscopy (AFM) (Cypher, Oxford Instruments) image was acquired in non-contact mode to confirm the number of layers in N-GQDs. The composition

of the sample was obtained from the energy-dispersive X-ray spectrometer (EDX) (Sigma, Zeiss). For EDX, an aqueous solution of the sample was drop-casted on a Si substrate covered with Aluminum foil. XRD pattern was recorded with Rigaku RINT 2500 TTRAX-III using Cu  $K_{\alpha}$  radiation with a scanning speed of 3°/min. Fourier transform infrared (FTIR) spectroscopy measurements were executed in PerkinElmer, Spectrum BX spectrophotometer with reflectance mode. Raman scattering measurements were performed in a Horiba Raman spectrometer (LabRam HR800, Jobin Yvon) at a laser excitation of 488 nm. For XRD, FTIR and Raman measurement, 50  $\mu$ L of sample were drop-casted on Si (100) wafer and dried at 50 °C and this process was repeated for 5 times. Using a commercial spectrophotometer (PerkinElmer, UV win Lab), UV–Vis absorption spectra of the samples were recorded. The steady-state photoluminescence (PL) measurements were performed by using a 300 nm excitation of Xe lamp of the spectrofluorometer (Horiba Jobin Yvon, Fluoromax-4). Time-resolved photoluminescence (TRPL) measurements were obtained with the excitation of 308 nm LED source by picosecond time-resolved luminescence spectrometer (Edinburg Instruments, Model: FSP920). UV–Vis, PL and TRPL spectra were collected in 3 ml quartz cuvette.

### 3. Results and discussions

#### 3.1. Morphology analysis

Fig. 1(a) shows the TEM image of as-prepared N-GQDs with homogeneous dispersion and the corresponding size distribution with lognormal fitting is depicted in the inset showing the average size of N-GQDs as 4.9 nm. In addition, a well-resolved lattice fringe pattern with interplanar spacing of 0.19 nm is observed from the HRTEM of the N-GQD (see Fig. 1(b)), corresponding to (101) hexagonal lattice plane of graphite. The AFM topographic image of as prepared N-GQDs is shown in Fig. S1 (Supporting Information) showing spherical N-GQDs consistent with the TEM images. AFM height profile of the N-GQDs shows its thickness 0.3–0.9 nm (see the inset of Fig. S1, Supporting Information) indicating that the N-GQDs contain about 1–3 layers of graphene. Fig. 1(c) shows the TEM image of hexagonal Au NPs successfully grown by using N-GQDs as a reducing agent, resulting to the Au@N-GQD hybrids formation. The inset of Fig. 1(c) shows the HRTEM lattice fringe of Au NPs with lattice spacing of 0.22 nm and 0.20 nm, corresponding to the Au(111) and Au(002) planes, respectively [25]. The sizes of Au NPs are in the range of 10–40 nm (see Fig. S2(a), Supporting Information). Further, the presence of N-GQDs (size 2–5 nm) on (111) facet of Au NP is observed in the HRTEM lattice image of Au@N-GQD, as shown in Fig. 1(d), and it reveals the decoration of N-GQDs on Au NP surface. The SAED pattern of N-GQD and Au@N-GQD shown in Fig. S2(b, c) (Supporting Information) also confirms the presence of different crystalline planes of graphitic carbon and Au crystal. The crystalline planes of graphitic carbon are marked with ‘G’. Fig. 1(e, f) show the high resolution TEM images of Au@N-GQD/DA after the addition of very low concentration of DA (0.06  $\mu$ M), where DA nicely wraps on Au@N-GQD. At a higher concentration (0.4  $\mu$ M DA), N-GQDs are observed to be detached partially from the Au NPs and decorated uniformly over the surrounding DA cloud, as demonstrated in Fig. 1(g). This may be due to the reduced interaction between Au NP and N-GQDs in presence of DA. Fig. 1(h, i) show the TEM images of Au@N-GQD with a higher concentration of DA (80  $\mu$ M) at different magnifications. Interestingly, at further higher DA concentration, Au NP and DA form a core-shell structure where Au NP and DA act as core and shell, respectively, as shown in Fig. 1(h, i). Interestingly, N-GQDs are observed to be completely detached from the Au NP surfaces and accumulate at the periphery of the DA shell. Note that in some regions, N-GQDs and DA clouds are found together away from the Au NPs (see Fig. 1(i)), which is very less compared to core-shell structures. The size distribution of N-GQDs in Au@N-GQD/DA composite is shown in the inset of Fig. 1(h), which shows the average particle size of 5 nm, consistent with

the size of precursor N-GQDs.

The atomic percentage of elements present and their spatial distribution were measured using EDX mapping. Fig. S3(a) (Supporting Information) shows the FESEM image of Au@N-GQD on which the elemental mapping was performed. Fig. S3(b–e) (Supporting Information) exhibit the spatial distribution of the elements Au, C, O, and N, respectively. As shown in Fig. S3(a–e) (Supporting Information), EDX elemental mapping corresponding to Au@N-GQD reveals that the Au NP is uniformly decorated with nitrogen-doped GQDs, which is consistent with the TEM analysis. However, due to the resolution limit of FESEM, the distribution of carbon elements in Fig. S3(c) does not show the outline of N-GQDs. Fig. S4(a–e) (Supporting Information) show the FESEM image of Au@N-GQD/DA and the spatial distribution of the elements Au, C, O, and N, respectively. Au NPs are observed to be decorated over the DA clouds. Note that DA and N-GQDs both contains carbon atoms. In addition, the EDX spectra corresponding to Au@N-GQD and Au@N-GQD/DA are shown in Figs. S3(f) and S4(f) (Supporting Information), respectively, confirming the elemental composition. It is quite likely that due to the carbon contamination during the FESEM measurement, the measured carbon contents in the samples are found to be relatively high. The higher carbon content in the S4(f) than that of S3(f) is consistent with the fact that DA contains carbon atoms.

#### 3.2. XRD analysis

The XRD patterns were recorded to confirm the structure and crystallinity of pristine DA, N-GQDs, Au@N-GQD and Au@N-GQD/DA and the results are shown in Fig. 2. In the pristine DA, two weak XRD peaks are detected at  $2\theta = 28.6^\circ$  and  $40.7^\circ$  corresponding to non-graphitic carbon (see Fig. 2(a)) [26]. In Fig. 2(b), a broad diffraction peak in N-GQDs detected at  $2\theta = 26.2^\circ$  is indexed as G (002) crystallographic plane of GQD due to  $sp^2$  hybridized carbon atoms and the broadening is due to the formation of quantum dots. Another weak peak detected at  $2\theta = 43.0^\circ$  is assigned to the G (100) plane of GQD arising from the functional groups [27]. Fig. 2(c) shows the XRD pattern of Au@N-GQD with the presence of G (002) peak of N-GQDs and three prominent peaks of face-centered-cubic (fcc) Au. The (002) plane of N-GQDs is detected at a slightly higher value ( $2\theta = 26.5^\circ$ ) supporting the contraction of the interplanar spacing of N-GQDs, which may be due to the interaction with Au NPs. The diffraction peaks at  $2\theta = 38.2^\circ$ ,  $44.5^\circ$ , and  $64.7^\circ$  are in agreement with the fcc phase structure of Au for (111), (002) and (220) planes, respectively [28]. Interestingly, the (100) peak of N-GQDs becomes very weak after their attachment with Au NPs, while, (101) peak appears significantly, as-shown in Fig. 2(c), which may be due to the change in orientation of the crystalline plane of N-GQDs after the interaction with metallic Au surfaces. With the addition of DA in Au@N-GQD, the G (002) diffraction peak is not clearly observed, may be due to the passivation by DA clouds. In addition, all the Au diffraction peaks are detected with slight peak broadening, indicating the formation of the Au@N-GQD/DA complex composite.

#### 3.3. Raman spectroscopy and FTIR analysis

Results of micro-Raman studies on different samples are shown in Fig. 3(a–c). To acquire the detailed information about the change in the crystalline orientation and attached functional groups, Raman spectrum of each sample is deconvoluted in the range 1000–1725  $cm^{-1}$  with Lorentz peaks. The respective peak positions and FWHMs are tabulated in Table T1 (Supporting Information). In case of as-grown N-GQDs, the deconvoluted peaks (see Fig. 3(a)) show the characteristic G band at 1576  $cm^{-1}$ , which is associated with the in-plane phonon vibration of  $sp^2$  carbon and D band at 1380  $cm^{-1}$  confirms the lattice distortions due to the oxygen functionalities [27,29–31]. The appearance of the other peaks in N-GQDs at 1094  $cm^{-1}$ , 1270  $cm^{-1}$ , and 1670  $cm^{-1}$  are due to the attached functional groups, associated with the stretching

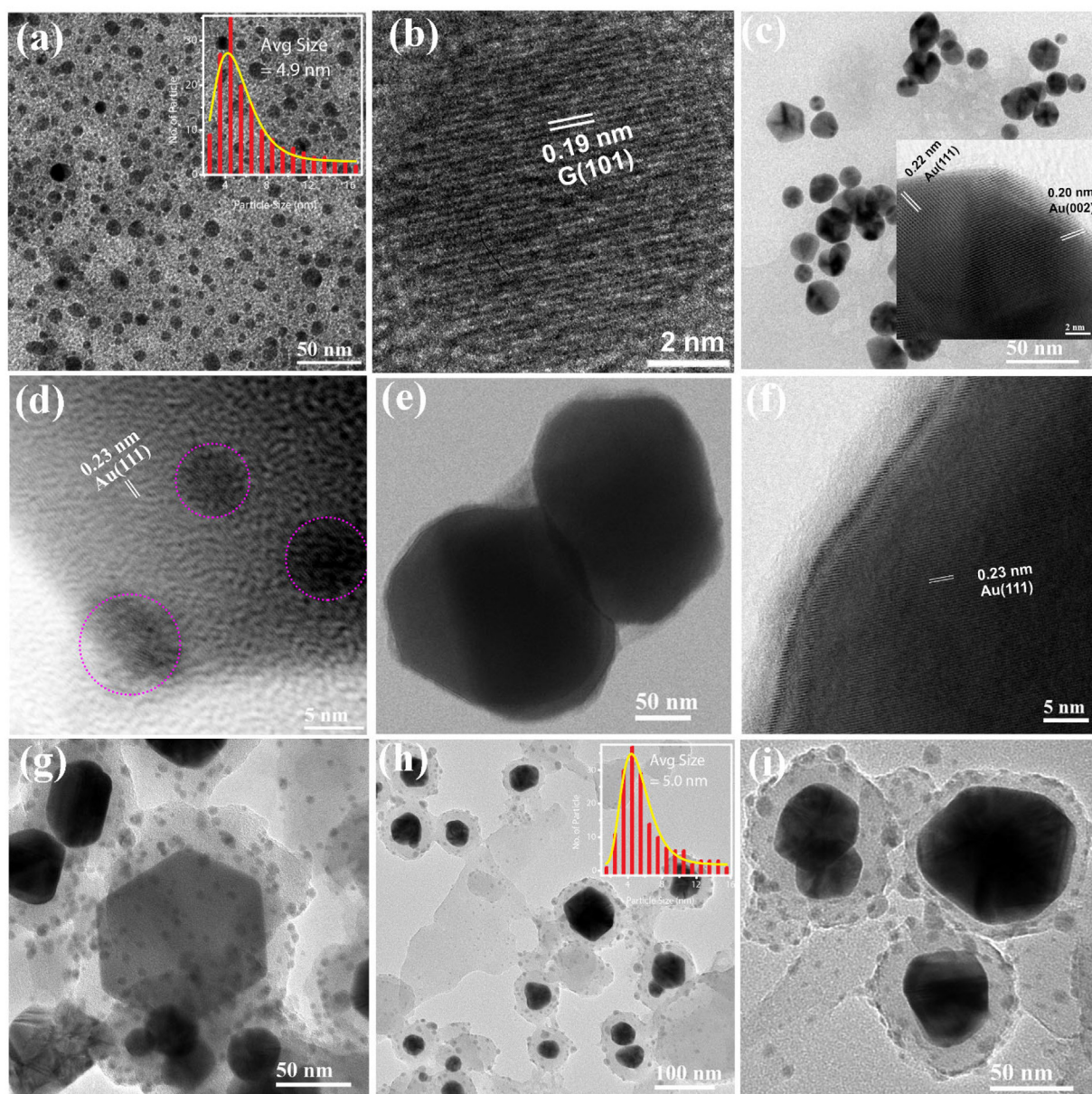


**Fig. 1.** (a) TEM image of N-GQDs with uniform size distribution shown as inset. (b) HRTEM of N-GQD with lattice spacing 0.19 nm. The IFFT (c) TEM image of Au@N-GQD hybrids with HRTEM of Au NP facets in inset. (d) HRTEM image of Au@N-GQD showing the decoration of N-GQDs (marked with dotted circles) on Au NP surface. TEM and HRTEM image of Au@N-GQD with different DA concentration: (e–f) 0.06  $\mu\text{M}$ , (g) 0.40  $\mu\text{M}$  and (h–i) 80  $\mu\text{M}$ . The inset of (h) shows the size distribution of N-GQDs at the periphery of the core-shell structure.

vibration of the C–C bond, tertiary dimethyl amines (C–N) group, and amide C=O bond, respectively [32]. As compared to N-GQDs, D band position in Au@N-GQD is red-shifted to  $1365\text{ cm}^{-1}$  (see Fig. 3(b)), due to the lattice distortion of N-GQDs caused by the local intensive plasmonic electromagnetic (EM) field induced by the Au NPs [33]. In contrast, G peak of Au@N-GQD is blue shifted by  $\sim 6\text{ cm}^{-1}$  with a drastic reduction of FWHM ( $\sim 87\text{ cm}^{-1}$ ) attributed to the strong vibration of C=C bond in graphitic component by the influence of Au NPs (see Table T1, Supporting Information). It is reported that due to the surface plasmon resonance (SPR) in Au NPs, local EM field enhancement increases, resulting in the intense absorption of incident light, following elastic scattering and the corresponding Raman signal enhancement, fully consistent with the present results [31,32]. In comparison with N-GQDs, the blue shift in G band in Au@N-GQD is attributed to the compressive strain in N-GQDs in presence of Au NPs, which is consistent with the XRD analyses. The upshift of the G-band is

reported to be associated with the charge transfer from N-GQDs to metallic NPs [31]. The Raman peaks of N-GQDs corresponding to the stretching vibration of the C–C bond are observed at  $1104\text{ cm}^{-1}$  for Au@N-GQD. Besides the characteristic D band and G band, the deconvoluted Raman spectrum of Au@N-GQD (see Fig. 3(b)) shows the appearance of different peaks at  $1104\text{ cm}^{-1}$  and  $1258\text{ cm}^{-1}$  with two new Raman active modes at  $1528\text{ cm}^{-1}$  and  $1629\text{ cm}^{-1}$ . The new peak at  $1528\text{ cm}^{-1}$  results from the lattice distortions in the  $\text{sp}^2$  plane of N-GQDs by the formation of Au–C bonds [34]. The other peak at  $1629\text{ cm}^{-1}$  in Au@N-GQD is assigned to the stretching vibration of C=N–OH, which confirms the additional functionalization of N-GQDs with O–H in the course of gold salt reduction [32]. Additionally, the peak at  $1258\text{ cm}^{-1}$  appeared in Au@N-GQD is attributed to the vibration of C–H bond. The Raman mode at  $1670\text{ cm}^{-1}$  of N-GQDs is observed to be disappeared after its interaction with Au NP surfaces, which may be due to the change of imines to –OH groups. The Raman

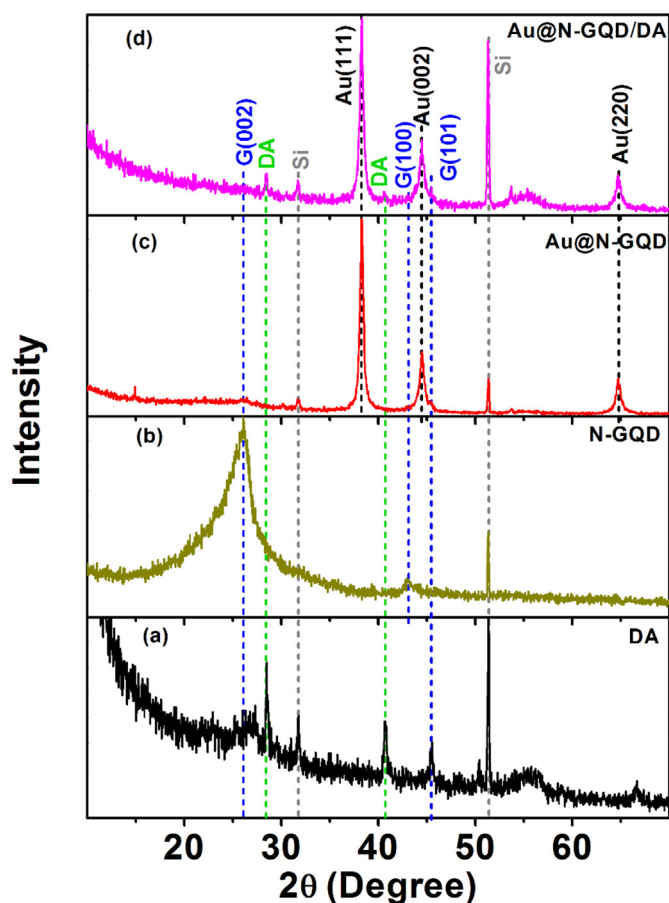


Fig. 2. XRD pattern of (a) pristine DA, (b) N-GQDs, (c) Au@N-GQD and (d) Au@N-GQD/DA. XRD pattern of each sample is recorded after the drop casting on Si (100) wafer.

spectrum of pristine DA with Lorentzian fittings is presented in Fig. S5(a) and the corresponding peak values are shown in Table T1 (Supporting Information). For Au@N-GQD/DA, the deconvoluted Raman spectrum shows the D band and G band position at  $1392\text{ cm}^{-1}$  and  $1583\text{ cm}^{-1}$ , respectively (see Fig. 3(c)). Raman modes observed at  $1338\text{ cm}^{-1}$  (stretching vibration of C–O bond) and  $1487\text{ cm}^{-1}$  (phenyl C=C stretching mode) confirm the attachment of DA with Au@N-GQD [35–37]. The D band position in Au@N-GQD/DA is observed to be upshifted from  $1365\text{ cm}^{-1}$  to  $1392\text{ cm}^{-1}$  as compared to the Au@N-GQD, which is due to the detachment of N-GQDs from Au NPs. This is further confirmed from the disappearance of the Au–C bond vibration ( $1528\text{ cm}^{-1}$ ) in Au@N-GQD/DA. Note that the value of  $I_G/I_D$  is  $\sim 2.5$  for Au@N-GQD/DA, while that for N-GQDs and Au@N-GQD is found to be  $\sim 1.3$ . The enhancement in G band intensity with DA addition may be attributed to the  $\pi$ - $\pi$  interaction and chemical bonding between N-GQDs and DA due to the presence of aromatic rings in both the systems [37,38]. In Au@N-GQD/DA, the Raman peak for C–C stretching vibration mode appears at  $1111\text{ cm}^{-1}$ , while C–N bending vibration mode of N-GQDs reappears at  $1277\text{ cm}^{-1}$  with a blue shift  $\sim 7\text{ cm}^{-1}$  confirming the partial detachment of N-GQDs from Au NPs.

The FTIR spectra were recorded (see Fig. 3(d–f)) to know the changes in the vibrational modes and chemical bonds before and after the addition of DA. A broad peak detected in the region  $3000$ – $3500\text{ cm}^{-1}$ , which is present in all the samples, can be attributed to the characteristic band of N–H stretching vibration and free hydroxyl group (O–H) vibration [39,40]. In case of N-GQDs (Fig. 3(d)), strong peaks detected at  $1651\text{ cm}^{-1}$  and  $1535\text{ cm}^{-1}$  correspond to the stretching and in-plane bending vibrations of the C–N bond, respectively, and it confirms the successful doping as well as the

functionalization of GQDs with nitrogen. The additional band at  $\sim 1253\text{ cm}^{-1}$  can be assigned as C–H<sub>2</sub> wagging vibration, while the other band in the region  $900$ – $1100\text{ cm}^{-1}$  is due to the stretching vibration of C–O group, confirming the presence of oxygen-rich functional groups in N-GQDs [32,40]. For Au@N-GQD composite (Fig. 3(e)), a strong as well as a sharp vibrational mode corresponding to C=C bond appears at  $1609\text{ cm}^{-1}$  due to the influence of SPR in Au NPs, fully consistent with the Raman analysis. As compared to N-GQDs, C–N bending mode in Au@N-GQD is observed to be down shifted from  $1535\text{ cm}^{-1}$  to  $1521\text{ cm}^{-1}$ , implying the attachment of N-GQDs with Au NPs by the C–N related functional groups. Additionally, a peak at  $1355\text{ cm}^{-1}$  corresponding to C–H/O–H bending vibration is observed in Au@N-GQD, which is in agreement with the Raman analysis. The presence of a strong and sharp band at  $475\text{ cm}^{-1}$  is due to the Au–C bond formation, which confirms the strong attachment of Au with N-GQDs [32,41]. In Fig. 3(f), the FTIR spectra of Au@N-GQD/DA shows two distinct peaks at  $1535\text{ cm}^{-1}$  and  $1682\text{ cm}^{-1}$  within a broad absorption band corresponding to C–N bending vibration, which is probably due to the CONH or CNH complex formation [32]. The absorption peak at  $1363\text{ cm}^{-1}$  arises from the vibration of O–H functional groups in DA (see Fig. S5(b), Supporting Information) and it disappears fully after the attachment with Au@N-GQD, while the appearance of the peak at  $1682\text{ cm}^{-1}$  corresponding to C=O vibration implies the conversion of catechol groups of DA into C=O bond in presence of Au@N-GQD. Interestingly, the reappearance of the absorption peak for C–N bending vibration in Au@N-GQD/DA at the identical position of that in N-GQDs ( $1535\text{ cm}^{-1}$ ) confirms the detachment of N-GQDs and Au NPs by the influence of DA, consistent with the TEM and Raman analysis. Note that in Au@N-GQD/DA, two absorption bands for C–O and C–H bond vibrations at  $\sim 1270\text{ cm}^{-1}$  and  $\sim 1343\text{ cm}^{-1}$ , respectively may result in peak broadening due to the influence of DA [32].

### 3.4. Mechanism of DA sensing

The bonding between Au NPs and N-GQDs has been confirmed from the XRD, RAMAN, FTIR and UV–Vis absorption, as discussed above. For the detection of DA with Au@N-GQD, here we propose a detailed mechanistic insight, as illustrated in Fig. 4. Before the addition of DA, there is a strong coupling/bonding between Au and N-GQD possibly through Au–C/C–N bonds. At lower concentration of DA, N-GQDs are detached from Au NPs and eventually it makes the N-GQD/DA complex. With further increase of the DA concentration, N-GQD/DA makes a shell like structure surrounding the Au NP. It has been reported that DA has good ionizing property due to the presence of two acidic protons with the value of approximately  $\sim 9\text{ pK}$  [42]. In a neutral medium, DA behaves as a positively charged particle with ( $-\text{NH}_3^+$ ) groups (known as protonated DA), while in N-GQDs, oxygen-rich functional groups, such as  $-\text{COOH}$ , C=O, C–O–C,  $-\text{OH}$  behave as negatively charged terminals [1,3,43]. Thus, high content of oxygen-rich functional groups at the edge as well as at the basal plane of N-GQDs can easily form a complex by neutralizing the amine group of protonated DA (CONH, CNH bond formation), whereas, the aromatic ring of N-GQDs and DA can also be attached by noncovalent interaction with  $\pi$ - $\pi$  stacking [1,15,37]. Due to the complex formation with DA, N-GQD/DA complex is forced to detach from Au NP surfaces and after the detachment of N-GQD/DA from the surface of Au NPs, electron density of Au NPs decrease. As a result, Au NPs become more active to accept electrons for recovering their electron density. Since DA is converted to protonated DA ( $\text{NH}_3^+$ ) in the neutral medium, the formation of stable dopamine-o-quinone (DQ) structure is not favorable for it [43]. After its attachment with N-GQDs, protonated DA becomes neutralized and may leave acidic protons of the catechol groups to get a stable structure of DQ via phenoxide-enolate formation [42]. Due to the high electron affinity, Au NPs readily accept the phenoxide-enolate through its negative charge terminal, forming a core-shell structure with Au NPs and DA, keeping N-GQDs at the periphery of the shell (see Fig. 1(i)). Note that the

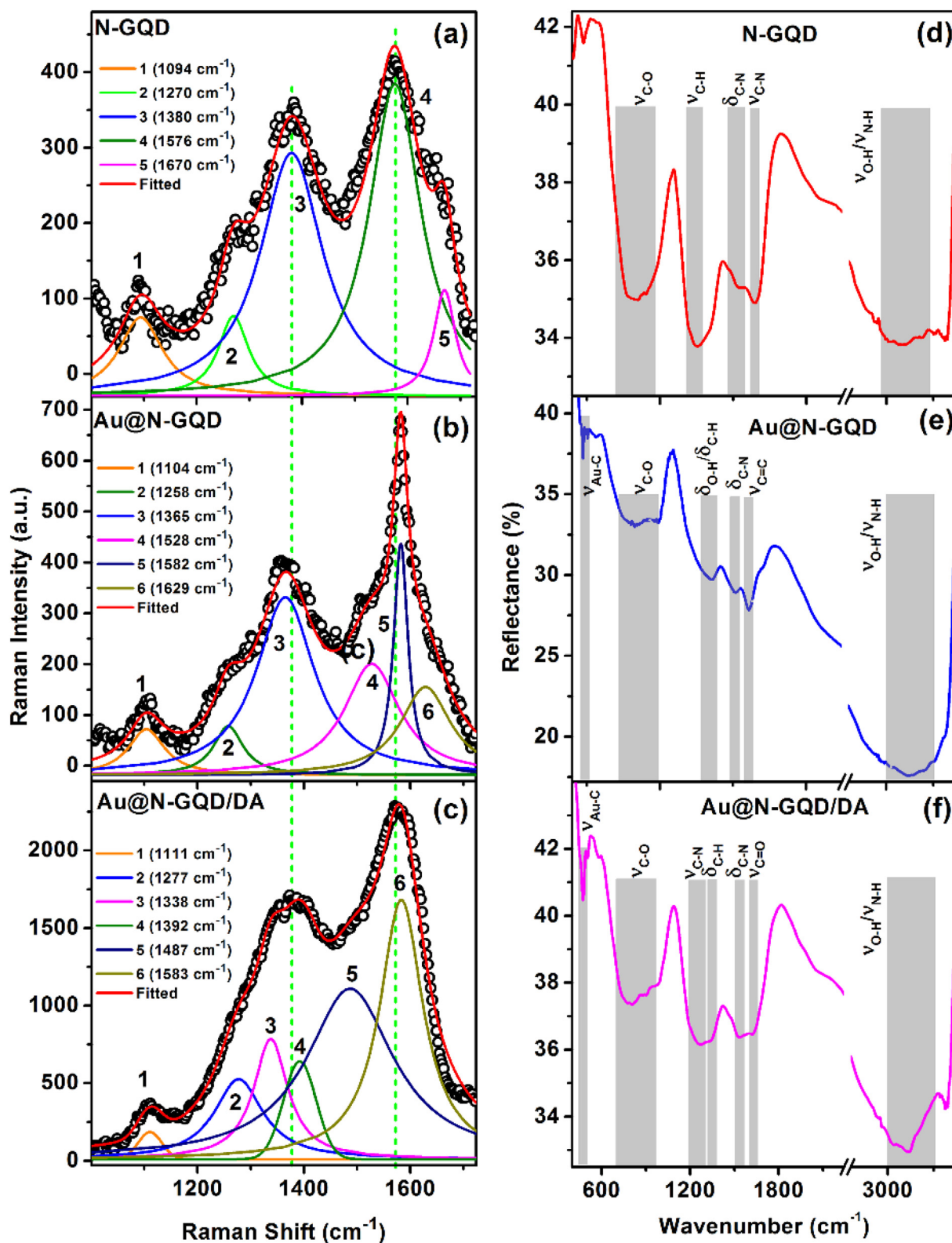


Fig. 3. (a–c) Comparison of Raman spectra and their Lorentzian fittings in the range 1000–1725  $\text{cm}^{-1}$  and (d–f) comparison of FTIR spectra of N-GQDs, Au@N-GQD and Au@N-GQD/DA, respectively.

detachment of the N-GQDs from Au NPs surfaces makes Au NP more active as an electron acceptor, accelerating complex formation between N-GQDs and DA. The quenching of PL intensity (discussed later) not only occurs through the ground state complex formation but also the charge transfer from N-GQDs to DQ takes place after certain

concentration of DA.

### 3.5. Colorimetric sensing of DA

Fig. 5(a) shows the comparison of UV–Vis absorption spectra of as

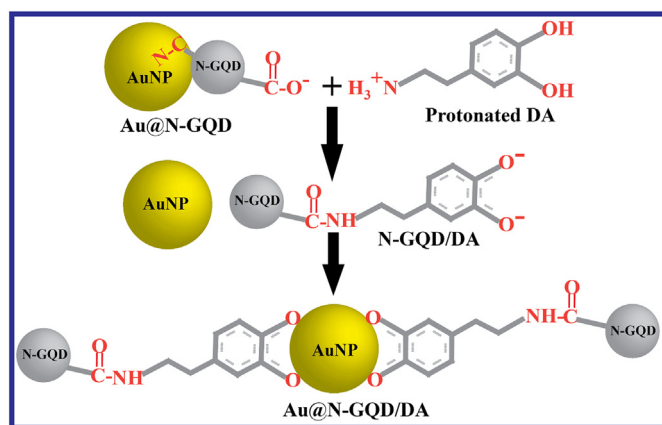


Fig. 4. A schematic illustration of the DA sensing mechanism showing the Au@N-GQD/DA complex formation through the detachment of N-GQDs from Au NPs, followed by the Au@N-GQD/DA core-shell structure with N-GQDs at the periphery.

prepared N-GQDs and Au@N-GQD. The absorption of N-GQDs is mainly dominant in the UV region with a hump at  $\sim 274$  nm due to the  $\pi$ - $\pi^*$  transition of  $sp^2$  hybridized carbon components, while an extended tail up to 650 nm is attributed to the  $n$ - $\pi^*$  transition arising from the non-bonding electrons of oxygen (CO=O, C=O or C-O) and lone pair electrons of nitrogen of the attached functional groups (C-NH<sub>2</sub>, C=NH) at N-GQDs edges [27,44]. For Au@N-GQD, two strong characteristic absorption peaks at  $\sim 300$  nm and  $\sim 543$  nm are observed (see Fig. 5(a)), which are attributed to the characteristic absorption peaks of N-GQDs and Au NPs, respectively. It is reported that the Au NPs with size 10–40 nm exhibit the SPR absorption at  $\sim 530$  nm [45]. However, in the present case the SPR absorption peak of Au NPs in Au@N-GQD is observed to be red shifted by  $\sim 13$  nm, which may be attributed to the hybrid formation of metallic Au NPs with N-GQDs [44]. The absorption peak at  $\sim 300$  nm in Au@N-GQD is stronger than that of N-GQDs, which may be due to the additional functionalization of N-GQDs during the formation of Au NPs, consistent with the Raman and FTIR studies. The ratio of HAuCl<sub>4</sub> and N-GQDs was optimized by monitoring the SPR absorption wavelength. In each case, the amount of N-GQDs was varied, keeping the HAuCl<sub>4</sub> concentration fixed. The variation of the SPR absorption peak position with the amount of reducing agent N-GQDs is plotted in Fig. S6 (Supporting Information). The smaller size of Au NPs are formed with 0.7 mg/mL of N-GQDs. Due to the higher surface area, smaller size Au NPs are more effective for the interaction. Thus, 0.7 mg/mL N-GQDs with 5 mM HAuCl<sub>4</sub> is chosen as optimum ratio for the further experiments.

For DA, the characteristic absorption peak for aromatic carbon (C=C) appears at 277 nm. Note that our sample does not show any peak at  $\sim 350$  nm (see Fig. S7(a), Supporting Information), indicating no oxidation of DA in our case [46,47]. After the addition of DA with Au@N-GQD (A7), a systematic enhancement in the intensity and the broadening of absorption peak at  $\sim 300$  nm is observed with increasing concentration of DA, as-shown in Fig. 5(b), which may be due to the complex formation of N-GQDs with DA. The enlarged view of the SPR absorption spectra (510–580 nm) of Au NPs in Au@N-GQD with different concentration of DA is presented in the inset of Fig. 5(b). The N-GQD/DA complex formation is supported by the shift in absorption peak of Au@N-GQD from 300 nm to 306 nm, as-shown in Fig. S7(a) (Supporting Information). Due to the complex formation with DA, the reduction of charge density in N-GQDs forces the detachment of N-GQD/DA complex from Au NP surfaces. As a result, with increasing the concentration of DA, electron density in Au NPs and the corresponding SPR absorption intensity is also reduced, while the absorption of N-GQDs ( $\sim 300$  nm) increases monotonically. Interestingly, further increase of DA concentration leads to the enhancement in the SPR

absorption intensity along with a redshift. The redshift of the SPR absorption peak may be due to the interaction of Au NPs with DA, while, the increased SPR absorption indicates the migration of electrons towards Au NPs [48]. Fig. 5(c) shows the change in the SPR absorption intensity ( $A_{543}$  at 543 nm) with different concentration of DA. After the detachment of the N-GQDs from Au NP surfaces, Au NPs become more active to recover the reduced electron density and as a result, they can actively attach with electron rich phenoxide-enolate, following more ground state complex formation between N-GQDs and DA, resulting in the enhancement of the absorption intensity at  $\sim 300$  nm. The variation of the absorption intensity spectra with DA concentrations were also repeated with two other stock solution of Au@N-GQD (A9 and A5) and the similar results are shown in Fig. S7(b, c) (Supporting Information). In order to support the role of Au NPs, the change in absorption of bare N-GQDs (N7) was also investigated in presence of different concentration of DA, as-shown in Fig. S7(d) (Supporting Information). Relatively higher absorption intensity with greater broadening is observed for Au@N-GQD, confirming the significant effect of the metallic Au NPs for the higher number of N-GQD/DA complex formation.

Based on the change in the absorption intensity at  $\sim 300$  nm, a novel sensor is proposed here for the detection of DA, following the well-known Hill equation. The Hill equation is a very useful tool in biochemistry and pharmacology to describe the binding of a ligand to a macromolecule. The Hill equation was originally formulated by Archibald Hill in 1910 to study the O<sub>2</sub> binding with haemoglobin [49]. Afterwards, Hill equation was well studied for analyzing the degree of cooperativity from Hill coefficient of ligand binding [50,51]. Arthur et al. used the Hill equation for fitting the curve of relative change in fluorescence with L-phenylalanine concentration [52]. According to the literature, the Hill equation is formally equivalent to Langmuir isotherm, while the Hill coefficient was reported as the interaction coefficient [53,54]. In order to study the detection of DA by Au@N-GQD hybrid system, the change in absorption intensity at  $\sim 300$  nm ( $A_{300}$ ) with various DA concentration is fitted with the following Hill equation,

$$A_{300} = S + \frac{(E - S)Q^n}{Q^n + K^n} \quad (1)$$

where, E, S, and K are the constants. Q is the concentration of DA and n is the interaction coefficient. If  $n > 1$ , the system shows positive cooperativity i.e. an increase in the affinity of a binding site due to the previous binding of a ligand to another site [55]. It is also reported that due to the multiple binding sites,  $n < 1$  is also possible for the binding of a ligand [56]. In case of the strong interaction,  $n > 1$  is observed. The plot of  $A_{300}$  vs. Q for each concentration of Au@N-GQD is well fitted by the Hill equation in the concentration region 0.1–10.0  $\mu$ M and the corresponding value of interaction coefficient are found to be  $n_{A9} = 0.97$ ,  $n_{A7} = 1.19$  and  $n_{A5} = 0.49$  for A9, A7 and A5, respectively (see Fig. 5(d)). It is evidence from the n values that the interaction is strong in case of A7. As compared to earlier reports, an efficient detection of DA with Au@N-GQD is carried out in this study in a wide a range (0.04–10  $\mu$ M), as listed in Table 1. The value of interaction coefficient (n) from the fitting with the Hill equation can be used for the prediction of optimum condition (concentration of Au@N-GQD stock solution) to achieve efficient DA sensing. For A9, as N-GQDs are less in amount, the absorption intensity corresponding to N-GQD/DA complex at  $\sim 300$  nm is low (see Fig. S7(b), Supporting Information), while for A5 the corresponding absorption is higher due to higher content of N-GQDs. Despite of a lower concentration of N-GQDs in A9, a larger value of interaction coefficient ( $n_{A9} = 0.97$ ) in A9 than that of A5 ( $n_{A5} = 0.49$ ) indicates the possibility of interaction of DA and Au NPs besides the interaction of DA and N-GQDs. In the dilute solution, as the amount of Au@N-GQD is less, these are well separated from each other and DA may easily separate N-GQDs from the Au NP surfaces by the formation of N-GQD/DA complex even at lower concentration of DA [1,57]. On the other hand, at the higher concentration of Au@N-GQD, metallic Au NP surfaces are highly crowded with N-GQDs and thus

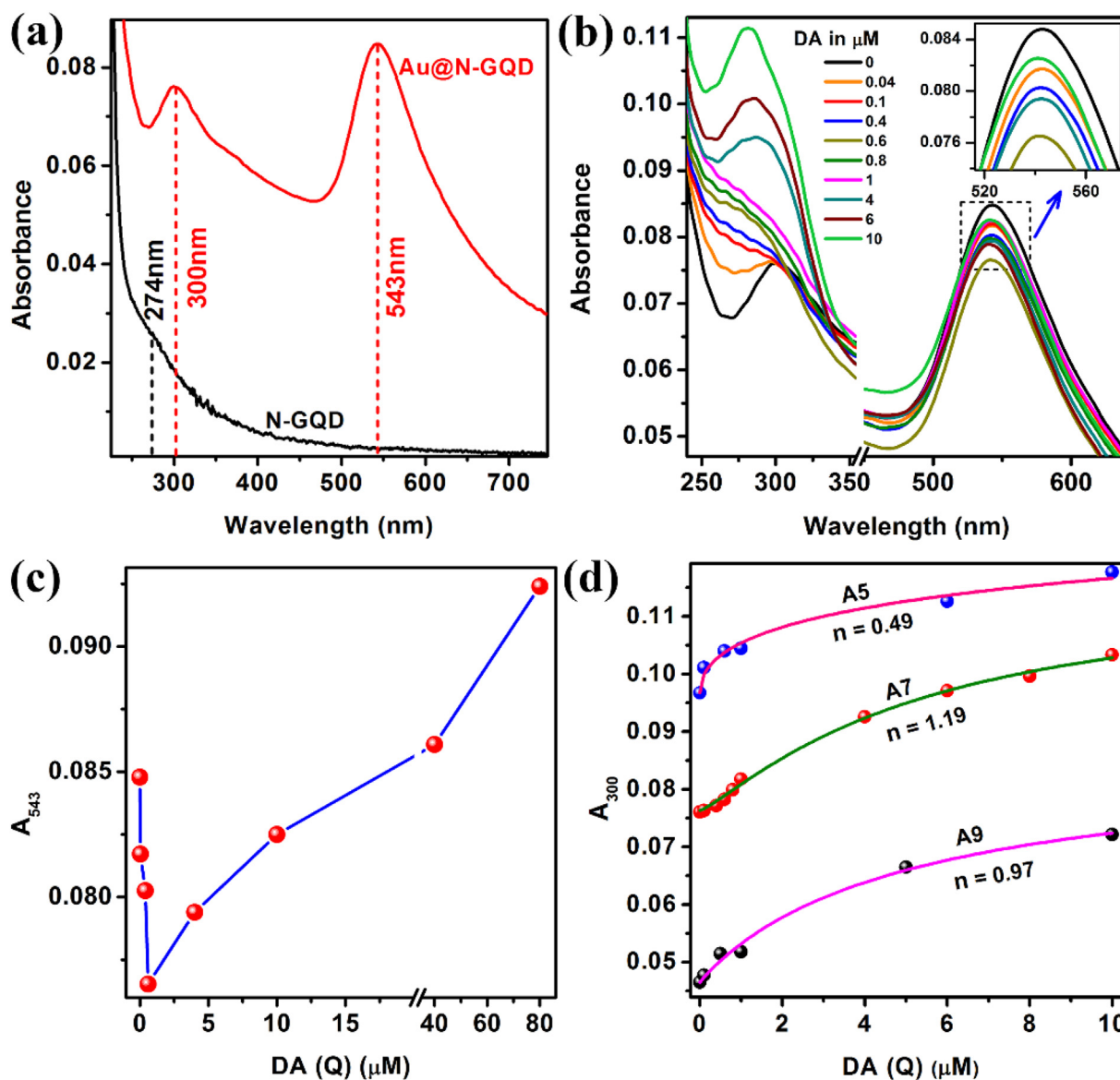


Fig. 5. UV-Vis absorption spectra of (a) N-GQDs and Au@N-GQD. (b) Au@N-GQD (A7) with various concentrations of DA (0–10  $\mu\text{M}$ ). (c) The change in SPR absorption intensity of Au@N-GQD at 543 nm with different DA concentrations. (d) Comparison of the change in absorption intensity of Au@N-GQD at 300 nm with different concentration of DA for A9, A7, and A5. Experimental data in each case is well fitted with the Hill equation and the corresponding  $n$  value is shown in each case.

higher concentration of DA is further involved in the N-GQD/DA complex formation than the interaction with Au NP surfaces. Thus, for A7 and A5, the higher absorption intensity at  $\sim 300$  nm indicates that

the absorption at  $\sim 300$  nm arises from the interaction between DA and N-GQDs. Though  $n$  value is decreasing with increasing concentration of Au@N-GQD stock solution, an intermediate concentration (A7)

**Table 1**  
Comparison of different colorimetric and fluorimetric sensors reported for DA detection.

Sensing platform	Sensing mechanism	Method of detection	Detection range	LOD (nM)	Reference
Au NP	Aggregation	Absorption	1.0 nM–1.0 $\mu\text{M}$	5000.0	[1]
Citrate cap-Ag NP	Aggregation	Absorption	0–0.6 $\mu\text{M}$	60.0	[3]
Au NP with $\text{Cu}^{+2}$	Aggregation	Absorption	0.5–10 $\mu\text{M}$	200.0	[2]
Beta-cyclodextrin modified Au NP	Aggregation	Absorption	20–250 nM and 350–1600 nM	3.0	[18]
Au@N-GQD	Core-shell formation	Absorption	0.04–80 $\mu\text{M}$	40.0	<i>This work</i>
GQD	Charge transfer	PL quenching	0.01–60 $\mu\text{M}$	8.0	[22]
GQD	Charge transfer	PL quenching	0.25–50 $\mu\text{M}$	90.0	[15]
N-GQD	Charge transfer	PL quenching	1–200 $\mu\text{M}$	70.0	[9]
Polypyrrole/GQD	Charge transfer	PL quenching	5–8000 nM	0.01	[4]
Dopamine modified Carbon NP with $\text{Fe}^{+3}$	Charge transfer	PL recovery	0.1–10 $\mu\text{M}$	68.0	[61]
Carbon Dot and Au NP	Aggregation of Au NP	PL recovery	0.5–3 $\mu\text{M}$	37.0	[23]
Au@N-GQD	Core-shell formation	PL quenching	0–100 $\mu\text{M}$	430.0	<i>This work</i>

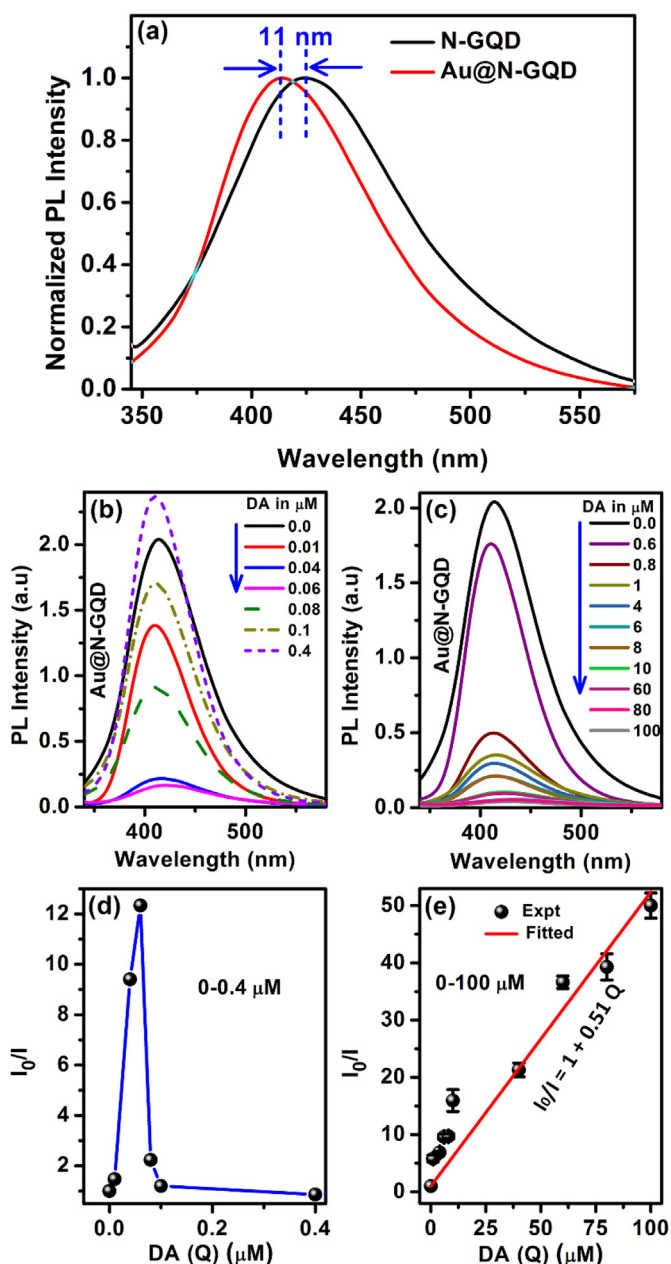


Fig. 6. (a) Normalized PL spectra of N-GQDs and Au@N-GQD, where vertical dashed lines indicate the blue shift of 11 nm with the addition of Au. A comparison of PL spectra of Au@N-GQD (A7) after the addition of DA in the concentration range (b) 0.0–0.4  $\mu\text{M}$  and (c) 0.6–100.0  $\mu\text{M}$  with the excitation wavelength 300 nm. The dashed/dotted lines in (b) indicate the non-monotonic change in the PL intensity with DA concentration. (d) The relative change in PL intensity ( $I_0/I$ ) as a function of DA concentration (for a fixed Au@N-GQD concentration (A7)) corresponding to the PL spectra of (b). (e)  $I_0/I$  vs concentration (Q) plot in the DA concentration range 1–100  $\mu\text{M}$  fitted with the linear Stern-Volmer equation. (For interpretation of the references to colour in this figure legend, the reader is referred to the web version of this article.)

between A9 and A5 shows a high interaction coefficient ( $n_{A7} = 1.19$ ) indicating high affinity of DA towards Au@N-GQD with an optimum concentration of Au@N-GQD (0.09 mg/mL). The highest value of  $n_{A7}$  confirms that Au NPs play an energetic role for the interaction between DA and N-GQDs. For A9 and A7, the SPR peak of Au NPs becomes broader and redshifted, whereas for A5 the SPR absorption intensity is increased without any shift. This may be explained by the better interaction of DA with Au NPs for A9 and A7, while for A5, mainly free

metallic Au NP surfaces are responsible for the enhanced SPR absorption. Thus, in order to achieve efficient detection of DA, the optimum concentration of Au@N-GQD is essential and in the present case, A7 is observed to be the optimum concentration.

### 3.6. Fluorescence sensing of DA

The efficient detection of DA based on the fluorescence intensity quenching of Au@N-GQD is carried out. The normalized PL spectra of Au@N-GQD show a blue shift of  $\sim 11$  nm as compared to the bare N-GQDs, as-shown in Fig. 6(a). The observed blue shift in the PL peak may be due to the addition of -OH groups on  $sp^2$ -hybridized carbons, which is in agreement with the FTIR analysis [58]. Fig. 6(b, c) shows the comparative PL spectra of A7 at various concentrations of DA (0–0.4  $\mu\text{M}$  and 0.6–100.0  $\mu\text{M}$ ). At very low concentration of DA, the PL intensity is found to be quenched and then PL intensity of the system is partially recovered with DA concentration in the range 0.08–0.40  $\mu\text{M}$  (see Fig. 6(b)). The dashed/dotted lines in Fig. 6(b) refer to the enhanced PL intensities of Au@N-GQD with DA addition. Interestingly, at the higher concentration of DA (0.6–100.0  $\mu\text{M}$ ) monotonic decrease in the PL intensity is observed, as-shown in Fig. 6(c) and this region of concentration is useful for DA sensing application. Fig. 6(d, e) depict the corresponding calibration graph of the fluorescence intensity ratio  $I_0/I$  vs. DA concentration (in  $\mu\text{M}$ ), where  $I_0$  and  $I$  are the PL intensity of the system at 414 nm before and after the addition of DA, respectively. For the detection of DA in the concentration range 1.0–100.0  $\mu\text{M}$ ,  $I_0/I$  vs. Q plot is fitted with a linear regression equation of:  $I_0/I = 1 + 0.51Q$ , as-shown in Fig. 6(e). The limit of detection (LOD), determined by the  $3\sigma/b$  ( $\sigma$  is the standard deviation of the lowest signal and  $b$  is the slope of linear calibration plot) is calculated to be 0.43  $\mu\text{M}$ , which is comparable with the reported values using fluorescence method. In our case the LOD value is consistent with the experimental observation, since the non-monotonic change in fluorescence intensity extends up to 0.40  $\mu\text{M}$  DA concentration and beyond it the linear sensing region starts. The details of the optimization of the fluorescence sensing parameters are provided in the Supporting information, section S1 and Figs. S8, S9. Based on the optimization, the sensing of DA has been carried out with sample A7 at pH 7 with temperature 30  $^\circ\text{C}$  after the 4 min proper mixing. In lower concentration region of DA, the covalent bond formation between  $-\text{NH}_3^+$  group of DA and oxygen coupled functional groups of N-GQDs facilitate a systematic reduction in the PL intensity by the ground state complex formation. PL quenching by electron transfer is negligibly small in the low concentration region (0.0–0.06  $\mu\text{M}$ ), which is confirmed by the TRPL analysis (discussed later). Due to the N-GQD/DA complex formation, N-GQDs are partially detached from Au NP surfaces, as discussed before. Thus, the exposed surface area of functionalized N-GQDs increases naturally and the PL starts to recover partially in the concentration region 0.08–0.4  $\mu\text{M}$  for A7. Beyond this concentration region, a dynamic PL quenching is observed up to 100.0  $\mu\text{M}$  DA concentration, evidenced by the TRPL studies. Besides the N-GQD/DA ground-state complex formation, Au NPs and DQ, being good electron acceptors may extract electrons from N-GQDs, which quench further the PL intensity in the higher concentration region.

To confirm the non-monotonic change in the PL intensity with DA, different stock solution of Au@N-GQD (A9 and A5) were also studied (see Fig. S10(a–d), Supporting Information). In each case, similar behavior is observed in the change of PL intensity with the variation of DA concentration. For A7 and A5, initially the PL intensity reduces systematically and then partially recovered, followed by the reduction in the PL intensity with increasing DA concentration. In case of A9, due to the presence of low concentration of N-GQDs, initially, PL recovers by the detachment of N-GQDs from Au NP surfaces and then quenches with higher DA concentration. For A5, in spite of the higher ground state complex formation, the involvement of more DA to make the surface of Au NPs free facilitates a lower interaction of Au NPs and

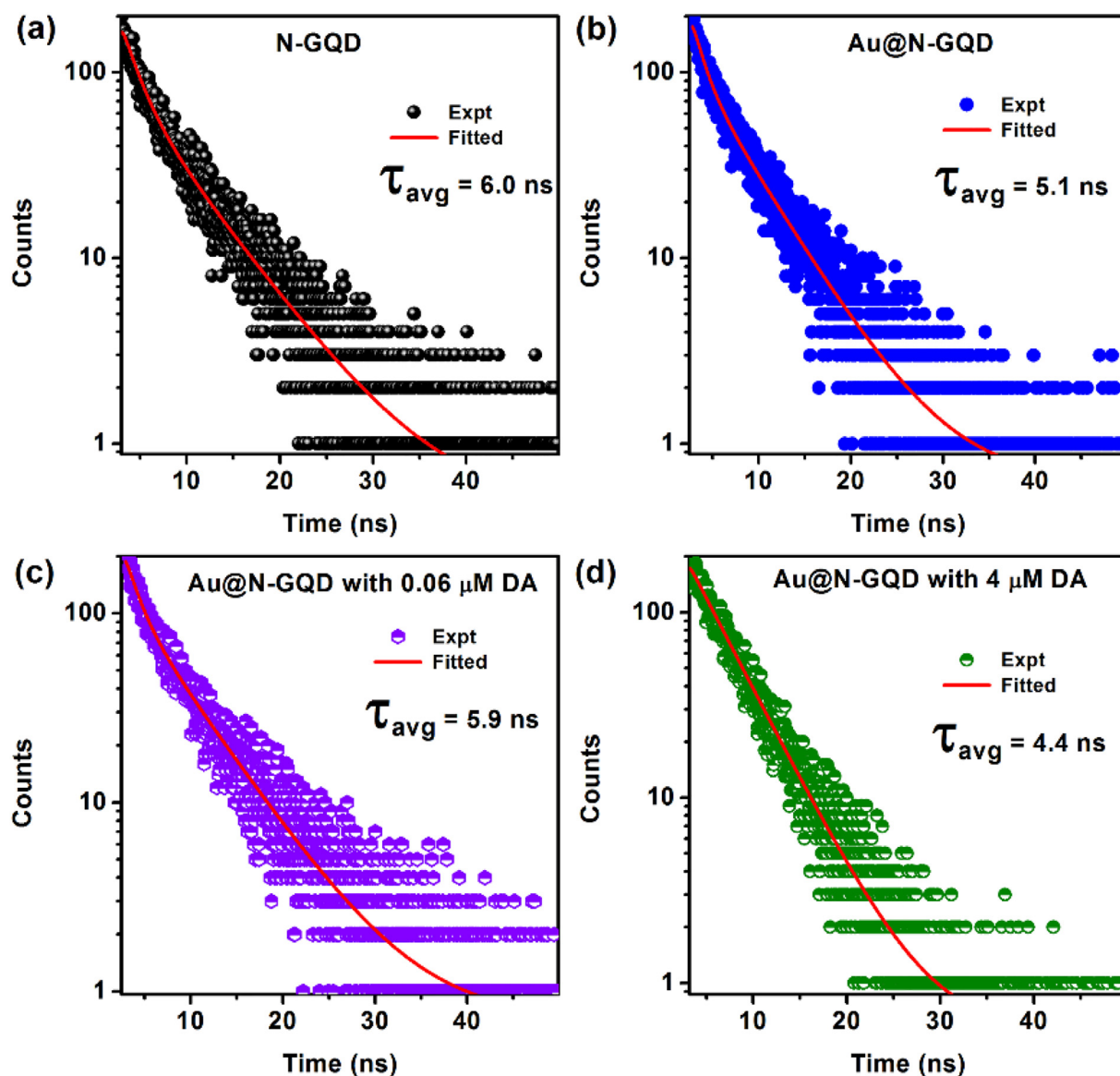


Fig. 7. TRPL spectra of (a) N-GQDs, (b) Au@N-GQD. (c) Au@N-GQD with 0.06  $\mu\text{M}$  DA, and (d) Au@N-GQD with 4.0  $\mu\text{M}$  DA.

phenoxide-enolate. A comparison of quenching study with N-GQDs and Au@N-GQD was performed to confirm our claim. Fig. S10(e) (Supporting Information) shows the monotonic quenching of PL intensity of N-GQDs with increasing concentration of DA. Fig. S10(f) (Supporting Information) shows the PL spectra of N-GQDs and Au@N-GQD with the DA concentration of 10  $\mu\text{M}$ . Quenching in PL intensity is measured to be  $\sim 1.57$  times and  $\sim 20.4$  times for N-GQDs and Au@N-GQD, respectively. Therefore, an enormous quenching in PL intensity is achieved in presence of Au@N-GQD, which can be treated as a superior fluorometric sensor for the detection of DA.

### 3.7. TRPL analysis

TRPL spectra for N-GQDs and Au@N-GQD before and after the addition of different concentration of DA were monitored at their respective emission peak. Each spectrum is fitted with the following bi-exponential decay function:

$$y(t) = B_1 e^{-\frac{t}{\tau_1}} + B_2 e^{-\frac{t}{\tau_2}} \quad (2)$$

where,  $\tau_1$  and  $\tau_2$  are the lifetime components with amplitude  $B_1$  and  $B_2$ , respectively, and  $t$  is the instantaneous time. The average decay time

( $\tau_{\text{avg}}$ ) is calculated with the formula:

$$\tau_{\text{avg}} = \sum_{k=1}^2 \frac{B_k \tau_k^2}{B_k \tau_k} \quad (3)$$

The bi-exponential decay behavior of the PL intensity suggests the presence of two emissive sites, which are usually attributed to the  $sp^2$  domains and functional groups at the edge of Au@N-GQDs [59]. The decay time including the corresponding amplitude and the average decay time of different systems are shown in Table T2 (Supporting Information). For N-GQDs,  $\tau_{\text{avg}}$  is calculated to be 6.0 ns, while that of Au@N-GQD is 5.1 ns, as-shown in Fig. 7(a, b), respectively. In the case of Au@N-GQD, electrons are transferred from N-GQDs to Au NPs due to the high electron affinity of Au NPs. The overlap of emission spectra of N-GQDs with the SPR absorption of Au NPs supports the possible electron transfer from N-GQDs to Au NPs [60]. In Au@N-GQD, the quenching of the PL by electron transfer is possible only when the radiative electrons of the system are transferred to other material or suffers from non-radiative recombination. With the lower concentration of DA (0.06  $\mu\text{M}$ ), negligible change in the decay time ( $\tau_{\text{avg}} = 5.9$  ns) of Au@N-GQD/DA as compared to N-GQDs confirms that the quenching in lower concentration region is only due to the ground state N-GQD/

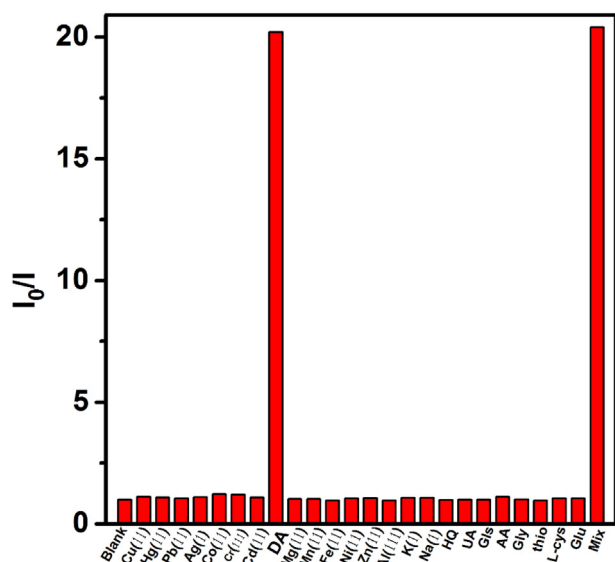


**Fig. 8.** Selectivity of DA sensing measured by fluorescence quenching ( $I_0/I$ ) of Au@N-GQD (0.09 mg/mL) at 414 nm in presence of 10  $\mu\text{M}$  concentration of different interference species.

DA complex formation (see Fig. 7(c)). At the higher concentration of DA, the high electron affinity of Au NPs and DQ facilitates the electron transfer from N-GQDs, which in turn results into fast decay time ( $\tau_{\text{avg}} = 4.4$  ns) for Au@N-GQD with 4  $\mu\text{M}$  DA, as-shown in Fig. 7(d). Thus, the presence of Au NPs accelerates the fast electron transfer resulting in the higher rate of complex formation and PL quenching.

### 3.8. Selectivity of DA sensing

For the detection of DA in real samples, not only the sensitivity but also the selectivity is very important because of the interference of different metal ions and biomolecules. In order to investigate the selectivity of the sensing, i.e., PL quenching and absorption intensity of Au@N-GQD towards DA, common interference species such as metal ions ( $\text{Ag}^+$ ,  $\text{Co}^{+2}$ ,  $\text{Cu}^{+2}$ ,  $\text{Hg}^{+2}$ ,  $\text{Pb}^{+2}$ ,  $\text{Cr}^{+3}$ ,  $\text{Al}^{+3}$ ,  $\text{Cd}^{+2}$ ,  $\text{Mg}^{+2}$ ,  $\text{Mn}^{+2}$ ,  $\text{Ni}^{+2}$ ,  $\text{Fe}^{+2}$ ,  $\text{Na}^+$ ,  $\text{K}^+$  and  $\text{Zn}^{+2}$ ) and biomolecules (ascorbic acid (AA), uric acid (UA), hydroquinone (HQ), glucose (Gls), glycine (Gly),

**Table 2**  
Detection of DA spiked in real samples.

Sample	Added concentration of DA ( $\mu\text{M}$ )	Measured concentration of DA ( $\mu\text{M}$ )	Recovery (%)	RSD (%)
Brahmaputra river water	10.0	$10.7 \pm 0.1$	107.0	0.9
	50.0	$48.2 \pm 0.5$	96.3	1.0
	80.0	$81.6 \pm 2.0$	102.1	2.5
Human serum	10.0	$11.2 \pm 0.2$	112.3	1.8
	50.0	$49.8 \pm 0.03$	99.6	0.1
	80.0	$75.6 \pm 0.1$	94.5	0.1

thiourea (thio), L-cysteine (L-Cys) and glutamic acid (Glu)) with the concentration of 10  $\mu\text{M}$  are considered under the identical experimental conditions. Fig. 8 shows the relative change of the PL intensity ( $I_0/I$ ) of Au@N-GQD with different species. The PL quenching occurs only with the addition of DA and no significant quenching is observed by the addition of other molecules and ions. The mixture of the all interference species with DA is also showing the similar quenching effect as with only DA. The selectivity of this hybrid system is also investigated by the change in the intensity of the absorption at 300 nm, as-shown in Fig. S11 (Supporting Information). These observations clearly confirm that proposed sensing platform is highly selective towards the detection of DA.

### 3.9. Analysis on real samples

For the investigation of the practical feasibility of Au@N-GQD based DA sensor, different concentration of DA in the range 0–80  $\mu\text{M}$  were spiked into real samples and the concentration of DA in the samples was determined by the standard addition method. The practicality of the proposed sensor is investigated as environmental sensor in Brahmaputra river water as well as biosensor in human serum sample, separately. Real water samples were collected from Brahmaputra River, Guwahati, Assam. The river water sample was simply filtered with a 0.22  $\mu\text{m}$  membrane without any further processing. For the detection of DA in river water, the detecting aqueous solution (Au@N-GQD) is prepared after 20 times diluting the filtered water with PBS buffer (pH 7). Similarly, another solution of Au@N-GQD is prepared in 100 fold diluted human serum sample. The change of the PL intensity with the spiked DA concentration in river water and serum sample,

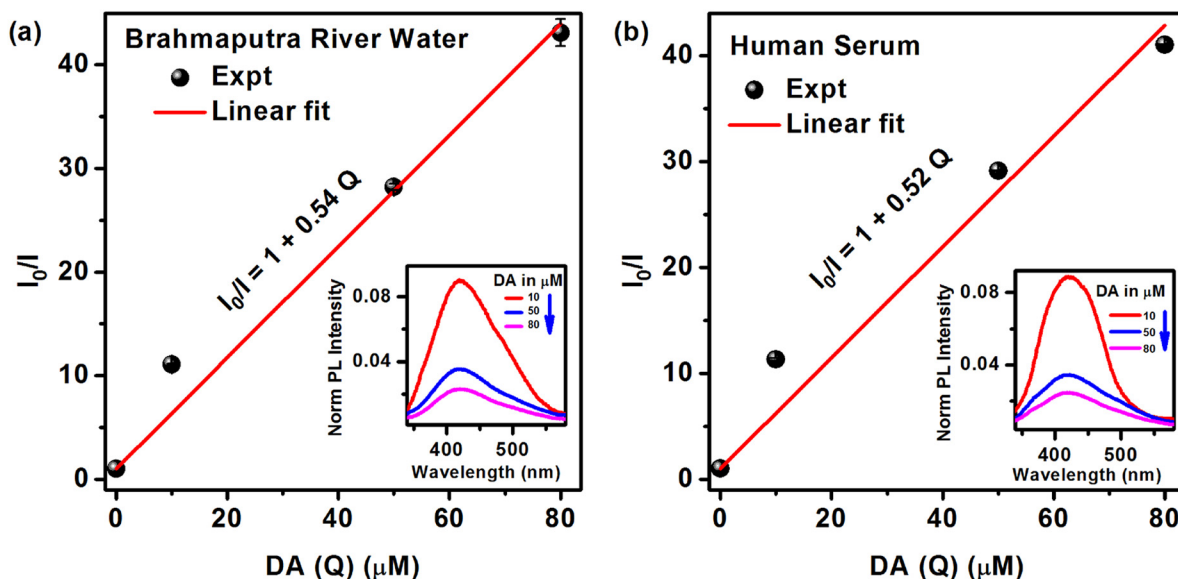


**Fig. 9.** The relative change of the fluorescence quenching ( $I_0/I$ ) of Au@N-GQD at 414 nm in presence of different concentration of DA spiked in (a) Brahmaputra river water and (b) human serum.

respectively, is shown in Fig. S12(a, b) (Supporting Information). The relative change in the PL intensity ( $I_0/I$ ) against spiked DA in river water and human serum follow the linear Stern-Volmer equation, as shown in Fig. 9(a, b) and the corresponding LODs are 480 nM and 590 nM, respectively (calculated at a signal-to-noise ratio of 3). The LOD for human serum sample is lower than the lowest abnormal DA concentration in human blood (16  $\mu$ M) [1]. The recovery of DA in the river water is 96.3–102.1% and that for human serum is 94.5–112.3%. With these low LOD and satisfactory recoveries in real medium, we can conclude that the proposed sensor is efficient and it holds potential for DA detection in environmental and biological samples with a fast and reproducible way. The calculations of spiked and recovery concentrations of DA in real medium are shown in Table 2.

#### 4. Conclusions

In summary, a unique simple photometric method has been utilized for the detection of DA below the abnormal level of DA in the human serum. The DA sensor is developed by integrating N-GQDs with Au NPs by the formation of a unique core-shell structure with DA, as revealed from the TEM analysis, for the first time. Here, Au NPs are demonstrated to play a pivotal role in the N-GQD/DA complex formation, which proves Au@N-GQD as a more efficient sensor than bare N-GQDs. Though primarily electrostatic interaction and  $\pi$ - $\pi$  stacking facilitate the N-GQD/DA ground state complex formation, the presence of Au NPs accelerates this ground state complex formation by making a core-shell structure with phenoxide-enolate. It is also highlighted that the core-shell structure helps for the greater quenching of PL intensity of Au@N-GQD by electron transfer. In presence of DA, the enhancement of UV-Vis absorption intensity and quenching of PL intensity of Au@N-GQD have been used for the colorimetric and fluorometric detection of DA in the range 0.04–100.0  $\mu$ M. Our results provide a detailed insight into the DA sensing through complex formation and core-shell structure generation with DA. This strategy offers a new approach for developing a simple, low cost, highly sensitive and selective DA sensor, useful in a wide range of applications in clinical diagnostics. The proposed sensor exhibits good reproducibility, simple operation and excellent stability. In addition, the proposed strategy was successfully applied for DA detection in Brahmaputra river water and human serum, achieving satisfactory recoveries and LOD. The observed DA shell formation around Au NPs and its evolution may serve as a guideline for further studies on core-shell formation in complex biomolecules.

#### Acknowledgments

We acknowledge the financial support from MEITY (Grant No. 5(9)/2012-NANO (VOL-II)) for carrying out part of this work. Central Instruments Facility, I.I.T. Guwahati is acknowledged for providing the TEM, FESEM, Raman and TRPL facilities.

#### Appendix A. Supplementary data

Supplementary data to this article can be found online at <https://doi.org/10.1016/j.apsusc.2019.06.065>.

#### References

- Y. Leng, K. Xie, L. Ye, G. Li, Z. Lu, J. He, Gold-nanoparticle-based colorimetric array for detection of dopamine in urine and serum, *Talanta* 139 (2015) 89–95.
- H. Su, B. Sun, L. Chen, Z. Xu, S. Ai, Colorimetric sensing of dopamine based on the aggregation of gold nanoparticles induced by copper ions, *Anal. Methods* 4 (12) (2012) 3981–3986.
- Y. Lin, C. Chen, C. Wang, F. Pu, J. Ren, X. Qu, Silver nanoprobe for sensitive and selective colorimetric detection of dopamine via robust Ag–catechol interaction, *ChemComm* 47 (4) (2011) 1181–1183.
- X. Zhou, P. Ma, A. Wang, C. Yu, T. Qian, S. Wu, et al., Dopamine fluorescent sensors based on polypyrrole/graphene quantum dots core/shell hybrids, *Biosens. Bioelectron.* 64 (2015) 404–410.
- L. Wu, L. Feng, J. Ren, X. Qu, Electrochemical detection of dopamine using porphyrin-functionalized graphene, *Biosens. Bioelectron.* 34 (1) (2012) 57–62.
- B. Guadarrama-Flores, M. Rodríguez-Monroy, F. Cruz-Sosa, F. García-Carmona, F. Gandía-Herrero, Production of dihydroxylated betalains and dopamine in cell suspension cultures of *Celosia argentea* var. *plumosa*, *J. Agric. Food Chem.* 63 (10) (2015) 2741–2749.
- A.-J. Wang, J.-J. Feng, W.-J. Dong, Y.-H. Lu, Z.-H. Li, M.-L. Riekkola, Spermine-graft-dextran non-covalent copolymer as coating material in separation of basic proteins and neurotransmitters by capillary electrophoresis, *J. Chromatogr. A* 1217 (31) (2010) 5130–5136.
- L. Yang, N. Huang, Q. Lu, M. Liu, H. Li, Y. Zhang, et al., A quadruplet electrochemical platform for ultrasensitive and simultaneous detection of ascorbic acid, dopamine, uric acid and acetaminophen based on a ferrocene derivative functional Au NPs/carbon dots nanocomposite and graphene, *Anal. Chim. Acta* 903 (2016) 69–80.
- X. Chen, S. Chen, Q. Ma, Fluorescence detection of dopamine based on nitrogen-doped graphene quantum dots and visible paper-based test strips, *Anal. Methods* 9 (15) (2017) 2246–2251.
- J. Yang, L.-S. Tang, R.-Y. Bao, L. Bai, Z.-Y. Liu, B.-H. Xie, et al., Hybrid network structure of boron nitride and graphene oxide in shape-stabilized composite phase change materials with enhanced thermal conductivity and light-to-electric energy conversion capability, *Sol. Energy Mater. Sol. Cells* 174 (2018) 56–64.
- S. Yu, L. Zhao, R. Liu, C. Zhang, H. Zheng, Y. Sun, et al., Performance enhancement of Cu-based AZO multilayer thin films via graphene fence engineering for organic solar cells, *Sol. Energy Mater. Sol. Cells* 183 (2018) 66–72.
- T. Soltani, A. Tayyebi, B.-K. Lee, Efficient promotion of charge separation with reduced graphene oxide (rGO) in BiVO<sub>4</sub>/rGO photoanode for greatly enhanced photoelectrochemical water splitting, *Sol. Energy Mater. Sol. Cells* 185 (2018) 325–332.
- G. Rajender, P.K. Giri, Formation mechanism of graphene quantum dots and their edge state conversion probed by photoluminescence and Raman spectroscopy, *J. Mater. Chem. C* 4 (46) (2016) 10852–10865.
- X. Hai, X. Lin, X. Chen, J. Wang, Highly selective and sensitive detection of cysteine with a graphene quantum dots-gold nanoparticles based core-shell nanosensor, *Sensors Actuators B Chem.* 257 (2018) 228–236.
- J. Zhao, L. Zhao, C. Lan, S. Zhao, Graphene quantum dots as effective probes for label-free fluorescence detection of dopamine, *Sensors Actuators B Chem.* 223 (2016) 246–251.
- S. Dey, A. Govindaraj, K. Biswas, C. Rao, Luminescence properties of boron and nitrogen doped graphene quantum dots prepared from arc-discharge-generated doped graphene samples, *Chem. Phys. Lett.* 595 (2014) 203–208.
- S.H. Jin, D.H. Kim, G.H. Jun, S.H. Hong, S. Jeon, Tuning the photoluminescence of graphene quantum dots through the charge transfer effect of functional groups, *ACS Nano* 7 (2) (2013) 1239–1245.
- D. Wen, W. Liu, A.K. Herrmann, D. Haubold, M. Holzschuh, F. Simon, et al., Simple and sensitive colorimetric detection of dopamine based on assembly of cyclodextrin-modified Au nanoparticles, *Small* 12 (18) (2016) 2439–2442.
- G. Goncalves, P.A. Marques, C.M. Granadeiro, H.I. Nogueira, M. Singh, J. Gracio, Surface modification of graphene nanosheets with gold nanoparticles: the role of oxygen moieties at graphene surface on gold nucleation and growth, *Chem. Mater.* 21 (20) (2009) 4796–4802.
- S.L. Ting, S.J. Ee, A. Ananthanarayanan, K.C. Leong, P. Chen, Graphene quantum dots functionalized gold nanoparticles for sensitive electrochemical detection of heavy metal ions, *Electrochim. Acta* 172 (2015) 7–11.
- J. Ju, W. Chen, In situ growth of surfactant-free gold nanoparticles on nitrogen-doped graphene quantum dots for electrochemical detection of hydrogen peroxide in biological environments, *Anal. Chem.* 87 (3) (2015) 1903–1910.
- S. Weng, D. Liang, H. Qiu, Z. Liu, Z. Lin, Z. Zheng, et al., A unique turn-off fluorescent strategy for sensing dopamine based on formed polydopamine (pDA) using graphene quantum dots (GQDs) as fluorescent probe, *Sensors Actuators B Chem.* 221 (2015) 7–14.
- F. Qu, W. Huang, J. You, A fluorescent sensor for detecting dopamine and tyrosinase activity by dual-emission carbon dots and gold nanoparticles, *Colloids Surf. B: Biointerfaces* 162 (2018) 212–219.
- J. Chen, B. Yao, C. Li, G. Shi, An improved Hummers method for eco-friendly synthesis of graphene oxide, *Carbon* 64 (2013) 225–229.
- T.J. Macdonald, K. Wu, S.K. Sehmi, S. Noimark, W.J. Peveler, H. Du Toit, et al., Thiol-capped gold nanoparticles swell-encapsulated into polyurethane as powerful antibacterial surfaces under dark and light conditions, *Sci. Rep.* 6 (2016) 39272.
- Y. Zhan, Z. Liu, Q. Liu, D. Huang, Y. Wei, Y. Hu, et al., A facile and one-pot synthesis of fluorescent graphitic carbon nitride quantum dots for bio-imaging applications, *New J. Chem.* 41 (10) (2017) 3930–3938.
- R. Das, G. Rajender, P.K. Giri, Anomalous fluorescence enhancement and fluorescence quenching of graphene quantum dots by single walled carbon nanotubes, *Phys. Chem. Chem. Phys.* 20 (6) (2018) 4527–4537.
- L. Cheng, X. Li, J. Dong, size-controlled preparation of gold nanoparticles with novel pH responsive gemini amphiphiles, *J. Mater. Chem. C* 3 (2015) 6334–6340.
- D.C. Marcano, D.V. Kosynkin, J.M. Berlin, A. Sinitski, Z. Sun, A. Slesarev, et al., Improved synthesis of graphene oxide, *ACS Nano* 4 (8) (2010) 4806–4814.
- V. Mochalin, S. Osswald, Y. Gogotsi, Contribution of functional groups to the Raman spectrum of nanodiamond powders, *Chem. Mater.* 21 (2) (2008) 273–279.
- B. Park, S.J. Kim, J.S. Sohn, M.S. Nam, S. Kang, S.C. Jun, Surface plasmon enhancement of photoluminescence in photo-chemically synthesized graphene quantum dot and Au nanosphere, *Nano Res.* 9 (6) (2016) 1866–1875.
- G. Socrates, *Infrared and Raman Characteristic Group Frequencies: Tables and Charts*, John Wiley & Sons, 2004.

- [33] C.-E. Cheng, C.-Y. Lin, H.-Y. Chang, C.-H. Huang, H.-Y. Lin, C.-H. Chen, et al., Surface-enhanced Raman scattering of graphene with photo-assisted-synthesized gold nanoparticles, *Opt. Express* 21 (5) (2013) 6547–6554.
- [34] R.K. Biroju, P.K. Giri, Defect enhanced efficient physical functionalization of graphene with gold nanoparticles probed by resonance Raman spectroscopy, *J. Phys. Chem. C* 118 (25) (2014) 13833–13843.
- [35] S. Sánchez-Cortés, J. García-Ramos, Adsorption and chemical modification of phenols on a silver surface, *J. Colloid Interface Sci.* 231 (1) (2000) 98–106.
- [36] L. Qin, X. Li, S.-Z. Kang, J. Mu, Gold nanoparticles conjugated dopamine as sensing platform for SERS detection, *Colloids Surf. B: Biointerfaces* 126 (2015) 210–216.
- [37] P. Wang, M. Xia, O. Liang, K. Sun, A.F. Cipriano, T. Schroeder, et al., Label-free SERS selective detection of dopamine and serotonin using graphene-Au nanopyramid heterostructure, *Anal. Chem.* 87 (20) (2015) 10255–10261.
- [38] X. Ling, L. Xie, Y. Fang, H. Xu, H. Zhang, J. Kong, et al., Can graphene be used as a substrate for Raman enhancement? *Nano Lett.* 10 (2) (2009) 553–561.
- [39] K.K. Paul, N. Srekanth, R.K. Biroju, T.N. Narayanan, P.K. Giri, Solar light driven photoelectrocatalytic hydrogen evolution and dye degradation by metal-free few-layer MoS<sub>2</sub> nanoflower/TiO<sub>2</sub> (B) nanobelts heterostructure, *Sol. Energy Mater. Sol. Cells* 185 (2018) 364–374.
- [40] H. Ren, D.D. Kulkarni, R. Kodiyath, W. Xu, I. Choi, V.V. Tsukruk, Competitive adsorption of dopamine and rhodamine 6G on the surface of graphene oxide, *ACS Appl. Mater. Interfaces* 6 (4) (2014) 2459–2470.
- [41] H.-T. Liu, X.-G. Xiong, P.D. Dau, Y.-L. Wang, D.-L. Huang, J. Li, et al., Probing the nature of gold–carbon bonding in gold–alkynyl complexes, *Nat. Commun.* 4 (2013) 2201.
- [42] S. Govindaraju, S.R. Ankireddy, B. Viswanath, J. Kim, K. Yun, Fluorescent gold nanoclusters for selective detection of dopamine in cerebrospinal fluid, *Sci. Rep.* 7 (2017) 40298.
- [43] A.N. Pham, T.D. Waite, Cu (II)-catalyzed oxidation of dopamine in aqueous solutions: mechanism and kinetics, *J. Inorg. Biochem.* 137 (2014) 74–84.
- [44] R. Gone, C. Biswajit, P.K. Giri, In situ decoration of plasmonic Au nanoparticles on graphene quantum dots-graphitic carbon nitride hybrid and evaluation of its visible light photocatalytic performance, *Nanotechnology* 28 (39) (2017) 395703.
- [45] Y.Q. He, S.P. Liu, L. Kong, Z.F. Liu, A study on the sizes and concentrations of gold nanoparticles by spectra of absorption, resonance Rayleigh scattering and resonance non-linear scattering, *Spectrochim. Acta A Mol. Biomol. Spectrosc.* 61 (13–14) (2005) 2861–2866.
- [46] Q. Wei, F. Zhang, J. Li, B. Li, C. Zhao, Oxidant-induced dopamine polymerization for multifunctional coatings, *Polym. Chem.* 1 (9) (2010) 1430–1433.
- [47] Y. Liu, K. Ai, J. Liu, M. Deng, Y. He, L. Lu, Dopamine-melanin colloidal nanospheres: an efficient near-infrared photothermal therapeutic agent for in vivo cancer therapy, *Adv. Mater.* 25 (9) (2013) 1353–1359.
- [48] K. Pashangeh, M.R. Hormozi-Nezhad, M. Akhond, G. Absalan, Laccase activity assay using surface plasmon resonance band of gold nanoparticles formed by dopamine, *Plasmonics* 13 (4) (2018) 1409–1415.
- [49] A.V. Hill, The possible effects of the aggregation of the molecules of haemoglobin on its dissociation curves, *J. Physiol.* 40 (1910) 4–7.
- [50] M.W. Pantoliano, E.C. Petrella, J.D. Kwasnoski, V.S. Lobanov, J. Myslik, E. Graf, et al., High-density miniaturized thermal shift assays as a general strategy for drug discovery, *J. Biomol. Screen.* 6 (6) (2001) 429–440.
- [51] R. Mattera, B. Pitts, M. Entman, L. Birnbaumer, Guanine nucleotide regulation of a mammalian myocardial muscarinic receptor system. Evidence for homo- and heterotropic cooperativity in ligand binding analyzed by computer-assisted curve fitting, *J. Biol. Chem.* 260 (12) (1985) 7410–7421.
- [52] A.D. Conigrave, S.J. Quinn, E.M. Brown, L-amino acid sensing by the extracellular Ca<sup>2+</sup>-sensing receptor, *Proc. Natl. Acad. Sci. U. S. A.* 97 (9) (2000) 4814–4819.
- [53] J.N. Weiss, The Hill equation revisited: uses and misuses, *FASEB J.* 11 (11) (1997) 835–841.
- [54] I. Langmuir, The adsorption of gases on plane surfaces of glass, mica and platinum, *J. Am. Chem. Soc.* 40 (9) (1918) 1361–1403.
- [55] D.I. Cattoni, O. Chara, S.B. Kaufman, F.L.G. Flecha, Cooperativity in binding processes: new insights from phenomenological modeling, *PLoS One* 10 (12) (2015) e0146043.
- [56] F.J. Ruzicka, P.A. Frey, Kinetic and spectroscopic evidence of negative cooperativity in the action of lysine 2,3-aminomutase, *J. Phys. Chem. B* 114 (49) (2010) 16118–16124.
- [57] Y. Bu, S. Lee, The optical properties of gold nanoparticles with dopamine at different hydrogen ion concentration, *J. Nanosci. Nanotechnol.* 13 (6) (2013) 4178–4182.
- [58] S. Hu, A. Trinchi, P. Atkin, I. Cole, Tunable photoluminescence across the entire visible spectrum from carbon dots excited by white light, *Angew. Chem.* 54 (10) (2015) 2970–2974.
- [59] Y. Zhao, X. Wu, S. Sun, L. Ma, L. Zhang, H. Lin, A facile and high-efficient approach to yellow emissive graphene quantum dots from graphene oxide, *Carbon* 124 (2017) 342–347.
- [60] S. Huang, L. Wang, C. Huang, B. Hu, W. Su, Q. Xiao, Graphene quantum dot coupled with gold nanoparticle based “off-on” fluorescent probe for sensitive and selective detection of L-cysteine, *Microchim. Acta* 183 (6) (2016) 1855–1864.
- [61] K. Qu, J. Wang, J. Ren, X. Qu, Carbon dots prepared by hydrothermal treatment of dopamine as an effective fluorescent sensing platform for the label-free detection of iron (III) ions and dopamine, *Chem. Eur. J.* 19 (22) (2013) 7243–7249.